ICNMM2012-73006

THERMAL TRANSPIRATION FLOW IN ANNULAR MICROCHANNELS

Peyman Taheri
Laboratory for Alternative Energy Conversion (LAEC)
Mechatronic Systems Engineering
School of Engineering Science
Simon Fraser University
Surrey, British Columbia, Canada
E-mail: ptaherib@sfu.ca

Majid Bahrami
Associate Professor
Mechatronic Systems Engineering
School of Engineering Science
Simon Fraser University
Surrey, British Columbia, Canada
E-mail: mbahrami@sfu.ca

ABSTRACT

Thermal transpiration flows of rarefied gases in annular channels are considered, where the driving force for the flow is a temperature gradient applied in the channel walls. The influence of gas rarefaction, aspect ratio of the annulus, and surface accommodation coefficient on mass and heat transfer in the process are investigated. For this, the linearized Navier–Stokes–Fourier (NSF) and regularized 13-moment (R13) equations are solved analytically, and a closed-form expression for Knudsen boundary layers is obtained. The results are compared to available solutions of the Boltzmann equation to highlight the advantages of the R13 over the NSF equations in describing rarefaction effects in this particular thermally-driven flow. Through comparisons with kinetic data it is shown that R13 equations are valid for moderate Knudsen numbers, i.e., Kn < 0.5, where NSF equations fail to describe the flow fields properly.

NOMENCLATURE

A	model dependent coefficient
B	model dependent coefficient
C	integrating constant
$\dot{e}$	heat flow rate [J s^{-1}]
F_e	thermodynamic force for heat transfer [J s^{-1}]
F_m	thermodynamic force for mass transfer [kg s^{-1}]
I	unit tensor
I_0	zeroth-order modified Bessel function of the first kind
$\tilde{J}_e$	dimensionless thermodynamic heat fluxes
$\tilde{J}_m$	dimensionless thermodynamic mass fluxes
K_0	zeroth-order modified Bessel function of the second kind
Kn	Knudsen number
L	channel length
ℓ	macroscopic length for flow
$\mathcal{L}$	arbitrary length
$\dot{m}$	mass flow rate [kg s^{-1}]
m	high-order moment tensor [N m^{-1} s^{-1}]
p	pressure [Pa]
Pr	Prandtl number
q	heat-flux vector
R	high-order moment tensor [N s^{-2}]
R	gas constant [J kg^{-1} K^{-1}]
r	radial coordinate
Δr	circular gap size [m]
T	temperature [K]
v	velocity vector
$\mathcal{V}$	slip velocity [m s^{-1}]
z	axial coordinate [m]

Greek

α	dimensional axial temperature gradient [J kg^{-1} m^{-1}]
δ	rarefaction parameter
ε	ratio of inner to outer radii
θ	temperature in energy unit [J kg^{-1}]
κ	thermal conductivity [kg m^{-1} s^{-1}]
λ	molecular mean free path [m]

μ	viscosity [kg m^{-1} s^{-1}]
ρ	mass density [kg m^{-3}]
$\boldsymbol{\sigma}$	stress deviator [Pa]
φ	azimuthal coordinate [Rad]
τ	dimensionless axial temperature gradient
χ	accommodation coefficient

Sub-/super-scripts

0	reference state
1	channel inlet
2	channel outlet
BGK	Bhatnagar−Gross−Krook model
i	inner cylinder
LB	linearized Boltzmann model
n	normal direction with respect to wall
NSF	Navier–Stokes–Fourier
o	outer cylinder
R13	Regularized 13-moment
T	transposed tensor
t	tangential direction with respect to wall
w	channel wall
~	dimensionless quantity

1. INTRODUCTION

In a rarefied gas confined in a channel or a pipe, when a temperature gradient is applied on the walls, a flow is induced in the direction of the temperature gradient, i.e., from cold to hot [1,2]. This pure thermally induced flow, initiates within a thin layer adjacent to the walls. However, as a result of shear stress diffusion, the thickness of this layer grows and flow eventually fills the width of the channel or pipe, if its length is sufficiently large. This phenomenon was first reported by Reynolds [3] in 1879 who named it *thermal transpiration flow*. At the same time, Maxwell [4] was trying to provide a microscopic description for this problem using kinetic theory of gases. Later experimental observations by Knudsen [5,6] proved the existence of a pumping effect in thermally-driven flows, so-called *thermomolecular pressure difference* (TPD) [7-12]. Recently, the possibility of using the pumping effect of thermal transpiration to create a microcompressor without moving parts (Knudsen compressor) has motivated rigorous experimental studies [13-15].

In gaseous flows, the measure for gas rarefaction is Knudsen number $Kn = \lambda / \ell$, the ratio of the molecular mean free path λ, and the geometric characteristic length of the flow ℓ. Accordingly, rarefied conditions are common in microsettings as well as in low-density (near vacuum) flows. Since in rarefied gas flows there are not sufficient collisions between the gas particles, an equilibrium state cannot be maintained, and the arising nonequilibrium effects alter the transport fields of mass and heat. It is evident that for rarefied gas flows the well

established laws of classical fluid dynamics, i.e., the laws of Navier−Stokes and Fourier (NSF), cease to be valid [16]. Consequently, nonequilibrium transport processes, including thermal transpiration flow, are mostly investigated numerically through kinetic models for the Boltzmann equation.

Thermal transpiration between two parallel plates is a well-known problem in kinetic theory, for which kinetic solutions obtained from Bhatnagar−Gross−Krook (BGK) model are reported in [17-21]. For this fundamental problem, more realistic kinetic data based on a linearized Boltzmann equation (LB) are also available in Refs. [22,23]. For circular channels, kinetic simulations of thermal transpiration was initiated by Sone and Yamamoto [24] and Loyalka [25] in 1968. Due to popularity of tubular flow passages in practical applications, their work was extended to study the effects of surface accommodation on mass and heat transfer of monatomic and polyatomic gases in thermally-induced flows [26-31]. An extensive bibliography and careful comparison of kinetic solutions for thermal transpiration is available in Ref. [32].

While kinetic solutions are very accurate, their complexity and computational cost limits their application, particularly in the engineering community. As alternatives to kinetic approaches, extended macroscopic transport equations which are derived from the Boltzmann equation can be used to describe rarefied gas flows at lower computational cost than the Boltzmann equation itself. This is done by reducing the degrees of freedom of the velocity distribution function, which is the main variable in the kinetic equation, to the degrees of freedom of a finite set of macroscopic variables. The Grad's moment expansion [33,34] and Chapman−Enskog expansion [35] are the classical methods to extract hydrodynamic-like equations from the Boltzmann equation.

In the present work, regularized 13-moment (R13) equations are used to describe transpiration flow of moderately rarefied gases in an annulus between two concentric cylinders. The R13 system is a regularized version of the classical Grad's 13-moment equations [16,36,37], suitable for flow simulation in the transition regime, $Kn \leq 1$. In contrast to Grad's 13-moment system, the R13 equations yield continuous shock structures at all Mach numbers [38], and correctly predict the formation of *Knudsen boundary layers* in fundamental boundary value problems for microflows [12,39-43]. Knudsen boundary layers are known as the dominant rarefaction effect in low speed rarefied gas flows.

Annular channels are considered in this study due to their specific geometrical property. When aspect ratio of the annulus (ratio of the inner cylinder radius to outer cylinder radius) is zero the problem represents thermal transpiration in tubes, and for annuli with aspect ratios close to unity the problem represents thermal transpiration in parallel plate channels (for sufficiently large radii).

In the following, linearized R13 equations are their boundary conditions [44] are adopted to describe thermally-induced flows in annular flow passages. For the considered problem, analytical solutions for linearized R13 and

Navier−Stokes−Fourier (NSF) equations are obtained and compared to some accurate kinetic data [45]. Through comparisons it is shown that due to capability of the R13 equations in capturing of rarefaction effects, which are missing in the NSF solutions, the R13 results match better with kinetic data. Our compact analytical solutions, which required modest computational effort, reveal that the presence of Knudsen boundary layers in the R13 solutions and their contribution to velocity slip is the main reason for this improvement.

2. FORMULATION OF THE PROBLEM

Monatomic ideal gases are considered with $p = \rho\theta$ as the equation of state, in which p, ρ, and $\theta = RT$ are pressure, mass density, and temperature in energy units (J kg^{-1}) respectively. The gas constant is R and T is the absolute temperature.

The flow configuration is shown in Fig. 1. The gas, confined in the annulus between two stationary coaxial cylinders, flows axially as a result of temperature variation along the cylindrical walls, i.e., *thermal transpiration flow*. Suggested by the channel geometry, it is appropriate to use cylindrical coordinates $\mathbf{x} = \{r, \varphi, z\}$, as shown in Fig. 1.

The pressure along the channel is a constant, p_0. The temperature of the walls at the inlet and outlet of the channel are θ_1^w and θ_2^w, respectively, with $\theta_1^w < \theta_2^w$. The superscript 'w' refers to the properties at the cylindrical walls. The temperature distribution in the walls is $\theta^w(z) = \theta_1^w + \alpha z$, where $\alpha = (\theta_2^w - \theta_1^w)/L$ is a positive and constant temperature gradient in the axial direction. The inner and outer radii of the circular gap are r_i and r_o, respectively. The aspect ratio of the annulus is $\varepsilon = r_i/r_o$ and the gap size is $\Delta r = r_o - r_i$. The length of the flow passage L, is assumed to be significantly large compared to its radial dimension, $L \gg \Delta r$, thus, boundary effects at entry and exit can be neglected, and the established temperature gradient in the gas and channel walls are the same.
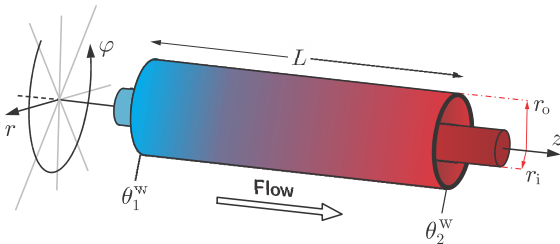

Fig. 1 Cylindrical coordinates and flow configuration in thermal transpiration flow between two coaxial cylinders of length L. The flow is driven by a constant temperature gradient in the axial direction, applied on both cylinders. Wall temperatures at the ends of the channel are θ_1^w and θ_2^w, with $\theta_2^w > \theta_1^w$. The annular gap size is $\Delta r = r_o - r_i$, and annulus aspect ratio is $\varepsilon = r_i/r_o$.

At this configuration a pure thermally-driven flow occurs from cold side of the channel to hot side. We investigate steady-state flow of the gas in the absence of external force

(e.g., gravity), driven by a constant and small temperature gradient in z-direction. Since the cylinders are not rotating, the flow is irrotational, $v_\varphi = 0$, and independent of the azimuthal direction, i.e., $\partial/\partial_\varphi = 0$.

It must be pointed that due to compressibility effects the actual flow in the annulus is two-dimensional in the *r-z* plane, which requires a numerical approach. Nevertheless, it is shown through kinetic simulations that for low Mach number flows through long capillaries, one can safely use "linear analysis" to discard the axial compressibility effects and simplify the problem such that a one-dimensional analysis suffices to investigate the local distribution of flow properties across the channel [12,32,42]. As discussed in Ref. [42], it is straightforward to show that a nonzero radial velocity v_r is a nonlinear effect due to compressibility effects, thus in our linear analysis $v_r = 0$ is considered.

3. REGULARIZED 13-MOMENT EQUATIONS IN LINEAR FORM

The derivations of regularized 13-moment (R13) equations and their corresponding boundary conditions for channel flows are discussed in [36,44]. The transformed equations and boundary conditions in cylindrical coordinates are presented in [12]; details on the transformation are available in Ref. [46].

In the present work, in order to obtain closed-form analytical solutions, linearized and steady-state equations are considered. For linearization, we consider a reference equilibrium state defined by p_0, $\theta_0 = (\theta_1^w + \theta_2^w)/2$, and $\rho_0 = p_0/\theta_0$ in which the gas is at rest, $\mathbf{v}_0 = 0$, and in equilibrium, i.e., $\mathbf{q}_0 = \boldsymbol{\sigma}_0 = 0$. The vectors $\mathbf{v}$ and $\mathbf{q}$ correspond to velocity and heat flux, while $\boldsymbol{\sigma}$ is the stress tensor deviator tensor.

The core equations in the R13 system are the main conservation laws for mass, momentum, and energy densities, which for the considered problem in steady state and linearized form read,

$$\nabla \cdot \mathbf{v} = 0, \tag{1}$$

$$\nabla \cdot \boldsymbol{\sigma} = 0, \tag{2}$$

$$\nabla \cdot \mathbf{q} = 0. \tag{3}$$

In the R13 system, stress deviator tensor $\boldsymbol{\sigma}$ and heat-flux vector $\mathbf{q}$ are given by their respective moment equations [16,36] that again in steady state and linearized form are

$$\frac{4}{5}\langle \nabla \mathbf{q} \rangle + \nabla \cdot \mathbf{m} = -2p_0 \langle \nabla \mathbf{v} \rangle - \frac{p_0}{\mu_0}\boldsymbol{\sigma}, \tag{4}$$

$$\theta_0 \nabla \cdot \boldsymbol{\sigma} + \frac{1}{2}\nabla \cdot \mathbf{R} = -\frac{5}{2}p_0 \nabla\theta - Pr\frac{p_0}{\mu_0}\mathbf{q}. \tag{5}$$

Here, μ_0 is the viscosity of the gas at the reference (equilibrium) state, and Pr is the Prandtl number.

Closure for Eqs. (1)–(5) is obtained from regularization [16,36], and leads to constitutive relations for higher-order moments $\mathbf{R}$ and $\mathbf{m}$, which in linear form read

$$\mathbf{R} = -\mathbf{A}\frac{\mu_0}{\rho_0}\langle\nabla\mathbf{q}\rangle, \qquad (6)$$

$$\mathbf{m} = -\mathbf{B}\frac{\mu_0}{\rho_0}\langle\nabla\sigma\rangle. \qquad (7)$$

In the above equations, terms inside angular brackets $\langle\cdots\rangle$ indicate the trace-free part of symmetric tensors. For instance, the trace-free part of the symmetric velocity gradient reads

$$\langle\nabla\mathbf{v}\rangle = \frac{1}{2}\left(\nabla\mathbf{v} + (\nabla\mathbf{v})^{\mathrm{T}}\right) - \frac{1}{3}\nabla\cdot\mathbf{v}\,\mathbf{I}, \qquad (8)$$

where the superscript 'T' indicates the transposed tensor, and $\mathbf{I}$ is the unit tensor. For the trace-free part of rank-3 tensors see Appendix A in Ref. [16].

The Prandtl number in the moment equation for heat flux, and the coefficients $\mathbf{A}$ and $\mathbf{B}$ in the constitutive are different in BGK kinetic model and linearized Boltzmann Equation model [16]. For the BGK kinetic model these coefficients are

$$Pr^{\mathrm{BGK}} = 1, \quad \mathbf{A}^{\mathrm{BGK}} = \frac{28}{5}, \quad \mathbf{B}^{\mathrm{BGK}} = 3, \qquad (9)$$

while for the linearized Boltzmann (LB) equation they read

$$Pr^{\mathrm{LB}} = \frac{2}{3}, \quad \mathbf{A}^{\mathrm{LB}} = \frac{24}{5}, \quad \mathbf{B}^{\mathrm{LB}} = 2. \qquad (10)$$

In the hydrodynamics limit where the high-order moments $\mathbf{R}$ and $\mathbf{m}$ vanish, the terms on the left-hand side of Eqs. (4) and (5) are zero, and they reduce to the linearized Navier–Stokes and Fourier laws of classical hydrodynamics, that is Newtonian viscous shear and Fourier's heat conduction,

$$\sigma = -2\mu_0\langle\nabla\mathbf{v}\rangle, \qquad (11)$$

$$\mathbf{q} = -\kappa_0\nabla\theta. \qquad (12)$$

with $\kappa_0 = 5\mu_0/(2Pr)$ as the thermal conductivity coefficient for ideal gas at the reference state. Equations (11) and (12) along with the conservation laws (1)–(3) form the linearized Navier–Stokes–Fourier system,

$$\nabla\cdot\mathbf{v} = 0, \quad \nabla^2\mathbf{v} = 0, \quad \nabla^2\theta = 0. \qquad (13)$$

4. WALL BOUNDARY CONDITIONS

For the considered boundary value problem, wall boundary conditions are required to relate properties of the gas (adjacent to the wall) to the wall temperature and the wall velocity. Since R13 equations are derived from the Boltzmann equation, it is natural to base the derivation of their boundary conditions on the boundary condition for the Boltzmann equation. Detailed discussion on derivation of wall boundary conditions for R13 equations is available in Refs. [44,46], where macroscopic boundary conditions for high-order moments are derived from Maxwell's boundary condition for the Boltzmann equation [4].

4.1. Boundary Conditions for the Regularized 13-moment Equations

The required boundary conditions for R13 system in linearized form are [42,44,46,47]

$$\sigma_{tn} = \frac{\chi}{2-\chi}\sqrt{\frac{2}{\pi\theta_0}}\left(-p_0\mathcal{V}_t - \frac{1}{5}q_t - \frac{1}{2}m_{tnn}\right), \qquad (14)$$

$$R_{tn} = \frac{\chi}{2-\chi}\sqrt{\frac{2}{\pi\theta_0}}\left(p_0\theta_0\mathcal{V}_t - \frac{11}{5}\theta_0 q_t - \frac{1}{2}\theta_0 m_{tnn}\right). \qquad (15)$$

The subscripts 't' and 'n' indicate *tangential* and *normal* directions with respect to the wall, that is the *z*- and *r*-directions, respectively [cf. Fig. 1]. The wall normal points in the radial direction toward the gas, thus, wall normal vectors have opposite signs on the inner and outer cylinders. Slip velocity on the wall is denoted by $\mathcal{V}_t$ and

$$\mathcal{V}_t = v_t - v_t^{\mathrm{w}}. \qquad (16)$$

The kinetic between the gas particles and wall surface is reflected in the surface accommodation coefficient χ, where $\chi = 0$ and $\chi = 1$ describe fully reflective (smooth) and fully diffusive (rough) walls, respectively.

As discussed in [42], additional boundary conditions for temperature, density, and normal components of heat flux and stress are required for the nonlinear R13 equations. Since in the present study we consider the linearized problem only, the boundary conditions required for the nonlinear setting are not shown.

4.2. Slip Condition for Navier–Stokes–Fourier Equations

Chapman–Enskog expansion of the quantities in boundary conditions (14) and (15), allows identifying their high-order terms. This general strategy is introduced in [48] to obtain a second-order velocity-slip condition for NSF system. In Appendix C of Ref. [46] this strategy is extended to derive second-order slip condition for curved boundaries. For axial

flows in cylindrical coordinates, the slip boundary condition in linear form reads [12]

$$\mathcal{V}_z^{\mathrm{NSF}} = -\frac{2-\chi}{\chi}\sqrt{\frac{\pi\theta_0}{2}}\frac{\sigma_{rz}^{\mathrm{NSF}}}{p_0}n_r - \frac{1}{5}\frac{q_z^{\mathrm{NSF}}}{p_0}$$
$$+\left[\left(\frac{1}{5Pr}+\frac{4\mathbf{B}}{15}\right)\frac{\partial\sigma_{rz}^{\mathrm{NSF}}}{\partial r}+\left(\frac{1}{5Pr}-\frac{\mathbf{B}}{15}\right)\frac{\sigma_{rz}^{\mathrm{NSF}}}{r}\right]\frac{\mu_0\theta_0}{p_0^2}.$$

(17)

The quantities $\sigma_{rz}^{\mathrm{NSF}}$ and q_z^{NSF} are the Navier–Stokes shear stress, Eq. (11), and Fourier's heat conduction, Eq. (12). The first and second terms represent the first-order slip velocity, and the rest are second-order corrections. The term $\sigma_{rz}^{\mathrm{NSF}}/r$ accounts for curvature effect of the channel wall. The wall normal is indicated by n_r, with $n_r = +1$ for the inner wall and $n_r = -1$ for the outer wall.

5. FLOW EQUATIONS

Flow equations for thermal transpiration in annular channels are obtained by transforming equations (1)–(7) and the NSF equations [cf. Eq. (13)] into cylindrical coordinates. Details on the transformation are available in Ref. [46]. For the considered flow configuration, as discussed in Section 2, the velocity vector $\mathbf{v}$, the heat-flux vector $\mathbf{q}$, and stress tensor $\boldsymbol{\sigma}$ simplify to

$$\mathbf{v} = \begin{pmatrix} 0 \\ 0 \\ v_z(r) \end{pmatrix}, \quad \mathbf{q} = \begin{pmatrix} q_r(r) \\ 0 \\ q_z(r) \end{pmatrix},$$
$$\boldsymbol{\sigma} = \begin{pmatrix} \sigma_{rr}(r) & 0 & \sigma_{rz}(r) \\ 0 & \sigma_{\varphi\varphi}(r) & 0 \\ \sigma_{rz}(r) & 0 & \sigma_{zz}(r) \end{pmatrix},$$

(18)

where all components only depend on the radial coordinate r. Since the stress tensor is trace free, we have $\sigma_{\varphi\varphi} = -\sigma_{rr} - \sigma_{zz}$, that confirms flow is completely independent of φ-direction.

The reference (equilibrium) state properties $\{p_0, \rho_0, \theta_0\}$ and an arbitrary length scale ℓ can be used to define dimensionless quantities. The radial and axial coordinates are normalized with respect to the length scale,

$$\tilde{r} = \frac{r}{\ell}, \quad \tilde{z} = \frac{z}{\ell}.$$

(19)

The remaining variables in dimensionless form are defined as

$$\tilde{\rho} = \frac{\rho}{\rho_0}, \quad \tilde{\theta} = \frac{\theta}{\theta_0}, \quad \tilde{p} = \frac{p}{p_0}, \quad \tilde{\mathbf{v}} = \frac{\mathbf{v}}{\sqrt{\theta_0}},$$
$$\tilde{\mathbf{q}} = \frac{\mathbf{q}}{p_0\sqrt{\theta_0}}, \quad \tilde{\boldsymbol{\sigma}} = \frac{\boldsymbol{\sigma}}{p_0}, \quad \tilde{\mathbf{R}} = \frac{\mathbf{R}}{p_0\theta_0}, \quad \tilde{\mathbf{m}} = \frac{\mathbf{m}}{p_0\sqrt{\theta_0}}.$$

(20)

The isothermal speed of sound $\sqrt{\theta_0}$ is used to scale the velocity. The tilde signs indicate dimensionless quantities.

Application of differential operators (divergences and gradients) in cylindrical geometry [46], and then, introduction of the above dimensionless quantities in Eqs. (1)–(7) yield the dimensionless form of the linearized R13 equations in cylindrical coordinates,

$$\left(\frac{\partial}{\partial\tilde{r}}+\frac{1}{\tilde{r}}\right)\tilde{\sigma}_{rz} = 0,$$

(21)

$$\frac{1}{2}\left(\frac{\partial}{\partial\tilde{r}}+\frac{1}{\tilde{r}}\right)\tilde{R}_{rz} = -\frac{Pr}{Kn}\tilde{q}_z - \frac{5}{2}\tau,$$

(22)

$$\frac{2}{5}\frac{\partial\tilde{q}_z}{\partial\tilde{r}}+\frac{\partial\tilde{m}_{rrz}}{\partial\tilde{r}}+\frac{\tilde{m}_{rrz}-\tilde{m}_{\varphi\varphi z}}{\tilde{r}} = -\frac{1}{Kn}\tilde{\sigma}_{rz} - \frac{\partial\tilde{v}_z}{\partial\tilde{r}},$$

(23)

where τ is the dimensionless temperature gradient along the axial direction (a positive quantity for the flow setting in Fig. 1),

$$\tau = \frac{\ell}{\theta_0}\frac{\partial\theta}{\partial z} = \frac{\partial\tilde{\theta}}{\partial\tilde{z}}.$$

(24)

In the dimensionless equations the reference viscosity μ_0 can be related to the reference molecular mean free path λ_0. Accordingly, the Knudsen number appears in the dimensionless equations as

$$Kn = \frac{\lambda_0}{\ell} \quad \text{with} \quad \lambda_0 = \frac{\mu_0\sqrt{\theta_0}}{p_0},$$

(25)

The Knudsen number is the measure for gas rarefaction.

Equations (21) is the linearized and dimensionless momentum balance [Eq. (2)] in axial direction. Equation (22) is the axial component of heat-flux balance [Eq. (5)] in linearized dimensionless form. Equation (23) is the tangential component of shear-stress balance [Eq. (4)]. The dimensionless high-order moments in (22) and (23) follow from Eqs. (6) and (7) as

$$\tilde{R}_{rz} = -\frac{1}{2}\mathbf{A}\,Kn\frac{\partial\tilde{q}_z}{\partial\tilde{r}}, \quad \tilde{m}_{rrz} = -\tilde{m}_{\varphi\varphi z} = \frac{2}{3}\mathbf{B}\,Kn\frac{\tilde{\sigma}_{rz}}{\tilde{r}}.$$

(26)

Note that in this flow setting $\tilde{m}_{rrz}$ and $\tilde{m}_{\varphi\varphi z}$ are curvature effects only, and will diminish when $r \to \infty$. The required boundary conditions for the problem are the same as in (14) and (15), that in dimensionless form and with proper coordinate-indicative indices read

$$\tilde{\sigma}_{rz} = \frac{\chi}{2-\chi}\sqrt{\frac{2}{\pi}}\left(-\tilde{\mathcal{V}}_z - \frac{1}{5}\tilde{q}_z - \frac{1}{2}\tilde{m}_{rrz}\right)n_r,$$

(27)

$$\tilde{R}_{rz} = \frac{\chi}{2-\chi}\sqrt{\frac{2}{\pi}}\left(\tilde{\mathcal{V}}_z - \frac{11}{5}\tilde{q}_z - \frac{1}{2}\tilde{m}_{rrz}\right)n_r.$$

(28)

As mentioned in Section 3, in the asymptotic limit of $Kn \to 0$ the balance equations for stress and heat flux [Eqs. (4) and (5)] reduce to Newtonian viscous shear and Fourier's heat conduction, respectively, which in linearized dimensionless form in cylindrical coordinates are

$$\tilde{\sigma}_{rz}^{\mathrm{NSF}} = -Kn \frac{\partial \tilde{v}_z}{\partial \tilde{r}}, \qquad \tilde{q}_z^{\mathrm{NSF}} = -\frac{5}{2} \frac{Kn}{Pr} \frac{\partial \tilde{\theta}}{\partial \tilde{z}}. \qquad (29)$$

Replacement of the above equations in (21)-(23) and setting $\tilde{R}_{rz} = \tilde{m}_{rrz} = \tilde{m}_{\varphi\varphi z} = 0$ gives the NSF equations for this problem, i.e.,

$$\left(\frac{\partial}{\partial \tilde{r}} + \frac{1}{\tilde{r}} \right) \frac{\partial \tilde{v}_z}{\partial \tilde{r}} = 0. \qquad (30)$$

Note that Eqs. (22) and (23) are automatically satisfied.

The required boundary condition for Eq. (30) is the slip condition (17) in dimensionless form,

$$\tilde{\mathcal{V}}_z^{\mathrm{NSF}} = \left(\frac{2-\chi}{\chi} \sqrt{\frac{\pi}{2}} \frac{\partial \tilde{v}_z}{\partial \tilde{r}} n_r + \frac{1}{2Pr} \tau \right) Kn$$
$$- \left[\left(\frac{1}{5Pr} + \frac{4\mathbf{B}}{15} \right) \frac{\partial^2 \tilde{v}_z}{\partial \tilde{r}^2} + \left(\frac{1}{5Pr} - \frac{\mathbf{B}}{15} \right) \frac{1}{\tilde{r}} \frac{\partial \tilde{v}_z}{\partial \tilde{r}} \right] Kn^2. \qquad (31)$$

The terms multiplied by Kn^2 are the second-order corrections to slip velocity.

6. RESULTS AND DISCUSSIONS

6.1. Analytical Solution for Regularized 13-moment Equation

Replacement of (26) into (22) and (23) and subsequent integration gives the following analytical solutions for shear stress $\tilde{\sigma}_{rz}$, axial heat flux $\tilde{q}_z$, and velocity $\tilde{v}_z$,

$$\tilde{\sigma}_{rz} = \frac{\mathbf{C}_1}{\tilde{r}}, \qquad (32)$$

$$\tilde{q}_z = \mathbf{C}_2 I_0 \left(\frac{2}{Kn} \sqrt{\frac{Pr}{\mathbf{A}}} \tilde{r} \right) + \mathbf{C}_3 K_0 \left(\frac{2}{Kn} \sqrt{\frac{Pr}{\mathbf{A}}} \tilde{r} \right) - \frac{5}{2} \frac{Kn}{Pr} \tau, \quad (33)$$

$$\tilde{v}_z = \mathbf{C}_4 + \frac{Kn}{Pr} \tau - \frac{\mathbf{C}_1}{Kn} \ln(\tilde{r})$$
$$- \frac{2}{5} \left[\mathbf{C}_2 I_0 \left(\frac{2}{Kn} \sqrt{\frac{Pr}{\mathbf{A}}} \tilde{r} \right) + \mathbf{C}_3 K_0 \left(\frac{2}{Kn} \sqrt{\frac{Pr}{\mathbf{A}}} \tilde{r} \right) \right]. \qquad (34)$$

The underlined terms indicate the solution of the NSF equations. In the above general solutions $\mathbf{C}_1$ to $\mathbf{C}_4$ are the integrating constants, that must be determined from the boundary conditions on both inner and outer walls. For the NSF solution the constants $\mathbf{C}_1$ and $\mathbf{C}_4$ can be obtained from the slip condition (31). For the R13 solution the required

boundary conditions are (27) and (28). The expressions for constants $\mathbf{C}_1$ to $\mathbf{C}_4$ are too bulky, hence are not shown here. These constants can be computed using analytical software packages such as Mathematica® or Maple®. It is important to mention that all constants linearly depend on the axial temperature gradient τ.

As given in (32), both R13 and NSF systems yield identical solution for shear stress. Equation (33) confirms that NSF yields heat flow only in presence of a temperature gradient, while the full R13 solution includes other terms that describe rarefaction effects, i.e., a heat flux which is not driven by temperature gradient. The zeroth-order modified Bessel functions I_0 and K_0 represent the Knudsen boundary layers. The R13 velocity solution shows that Knudsen layers contribute in the flow velocity. This effect is missing in the NSF velocity solution.

For $\chi = 1$, $\varepsilon = 0.1$, and $Kn = \{0.05, 0.15, 0.3\}$ the solutions (32)–(34) are plotted in Fig. 2, which are normalized with respect to the temperature gradient. The results are obtained for both BGK and LB coefficients, as given in Eqs. (9) and (10). The slip conditions for NSF yields $\mathbf{C}_1 = 0$. Accordingly, $\tilde{\sigma}_{rz}^{\mathrm{NSF}} = 0$ and the second-order slip condition reduces to

$$\tilde{\mathcal{V}}_z^{\mathrm{NSF}} = \frac{1}{2} \frac{Kn}{Pr} \tau. \qquad (35)$$

Due to this simplification, the effects of accommodation coefficients and second-order slip terms cannot be captured for NSF equations in linear analysis.

Fig. 2 (a) shows shear stress distribution in the annular gap between $r_i / \Delta r = \varepsilon / (1-\varepsilon)$ and $r_o / \Delta r = 1 / (1-\varepsilon)$. In contrast to the NSF, the constant $\mathbf{C}_1$ does not vanish in the R13 solution and the predicted shear stress is non-zero. However, in the hydrodynamic limit when $Kn \to 0$ the R13 shear stress converges to that of NSF. As the Knudsen number increases, the solutions with LB coefficients yield higher shear stress on the inner wall, compared to BGK coefficients. Unfortunately, kinetic data (solutions of the Boltzmann equation) for shear stress is not reported in the literature to perform a comparison, and evaluate the accuracy of our results.

Fig. 2 (b) shows the heat flux distribution across the channel. As given in Eq. (33), NSF predicts a uniform heat flow in the opposite direction of the temperature gradient, postulated by Fourier's law. For $Kn = 0.05$ the R13 solution differs to the NSF only on the narrow region close to the boundaries, which is the effect of Knudsen boundary layers, i.e., the terms with Bessel functions. As the Knudsen number increases the thickness of Knudsen layers increases; for $Kn = \{0.15, 0.3\}$ the Knudsen layers affect the whole cross section. The heat flow in Knudsen layers competes with Fourier heat flow, i.e., it occurs in the direction of temperature gradient. The magnitude of heat flow predicted by LB model is considerably larger than BGK model, mainly due to the difference in Prandtl numbers. Kinetic

data for the isothermal heat flux are not available for comparison. The validity of our heat-flux solutions are discussed in the next section, where the thermal energy flow rate is evaluated from NSF and R13 solutions and compared to kinetic data.
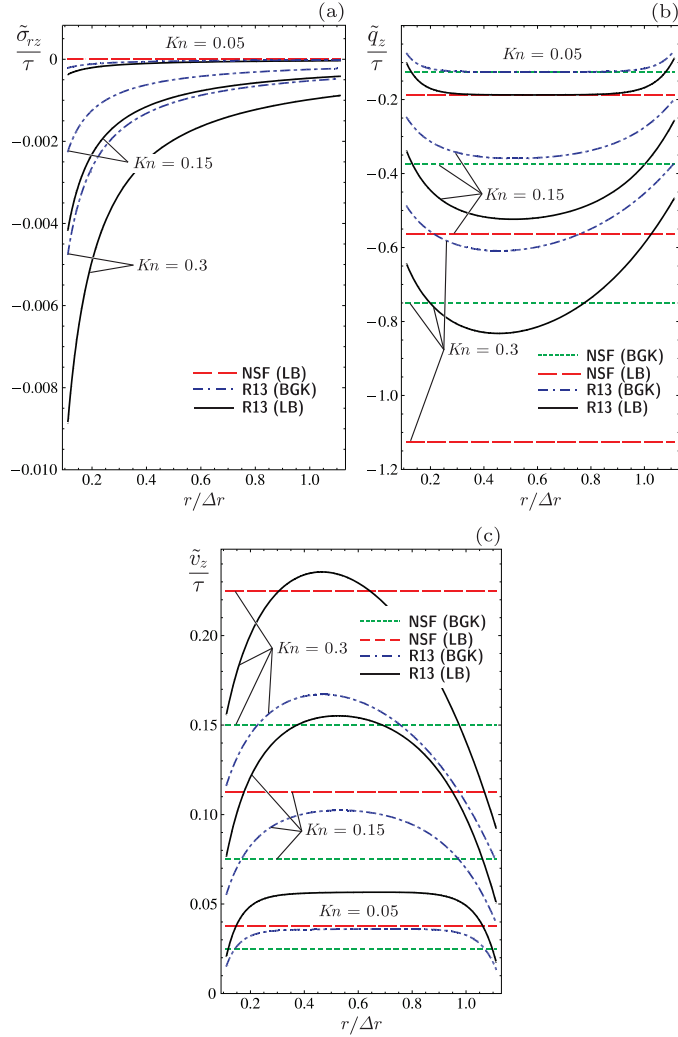

Fig. 2: Normalized distribution of shear stress, heat flux, and velocity across the annulus are plotted. The plots are obtained for coefficients for $\chi = 1$ and $\varepsilon = 0.1$, with both BGK and LB coefficients. Solutions for NSF and R13 are compared for $Kn = \{0.05, 0.15, 0.3\}$.

Fig. 2 (c) shows the velocity profiles. Similar to heat flux, velocity distribution is uniform in the NSF solution. The term $C_1 \ln(\tilde{r})/Kn$ in (34) which represent asymmetric velocity distribution due to curvature, vanished in the NSF solution because $C_1 = 0$. The validity of the R13 velocity solution and the effects of Knudsen layers contribution are discussed in the next section, where the mass flow rate is evaluated from NSF and R13 solutions and compared to kinetic data.

To show the influence of the annulus aspect ratio and surface accommodation coefficient in the process, solutions for

$Kn = 0.15$, $\varepsilon = \{0.2, 0.9\}$, and $\chi = \{0.6, 0.8, 1\}$ are plotted in Fig. 3. For the plots the LB coefficients in Eq. (10) are employed. For $\varepsilon = 0.2$, i.e., left plots in Fig. 3, the curvature difference between the inner and outer walls is significant, and R13 profiles are asymmetric with respect to the centerline of the annulus. For larger values of ε, when the size of the gap decreases and surface curvatures become close, the curvature difference effects vanished and solutions converge to the planar geometry results [42]. As shown in the right-hand side plots, for $\varepsilon = 0.9$ the stress distribution converges to linear distribution (with very small magnitudes), and heat flux and velocity distributions are almost symmetric. Fully dissuasive wall with $\chi = 1$ exhibit more friction, hence, at the walls, stress increases with χ, but heat flux and velocity decrease.
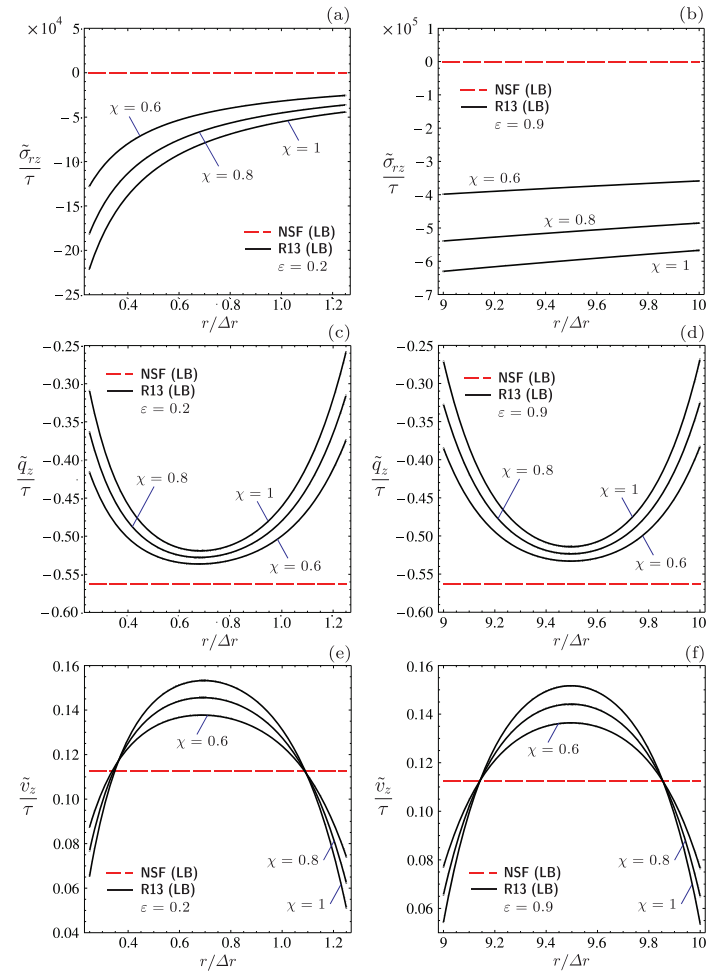

Fig. 3: Normalized distributions of shear stress, heat flux, and velocity across the annulus are compared between NSF and R13. The plots are obtained for $Kn = 0.15$, $\chi = \{0.6, 0.8, 1\}$, and $\varepsilon = \{0.2, 0.9\}$, with LB coefficients.

6.2. Mass and Thermal Energy Flow Rates: Comparison with Kinetic Data

Following the work of Lo *et al.* [45], flow rates for mass $\dot{m}$ (kg s^{-1}) and heat $\dot{e}$ (J s^{-1}) in transpiration flow can be expressed by phenomenological laws (for the linear case)

$$\dot{m} = F_m \tilde{J}_m, \qquad \dot{e} = F_e \tilde{J}_e \qquad (36)$$

where F_m and F_e are the thermodynamic force for mass and heat transfer, respectively, and $\tilde{J}_m$ and $\tilde{J}_e$ are the corresponding dimensionless thermodynamic fluxes of mass and heat. The thermodynamic forces, which include the temperature gradient, are [45]

$$F_m = -2\sqrt{2}\,\pi \mathcal{L}^3 \frac{\rho_0}{\sqrt{\theta_0}}\frac{\partial \theta}{\partial z}, \quad F_e = -2\sqrt{2}\,\pi \mathcal{L}^3 \frac{p_0}{\sqrt{\theta_0}}\frac{\partial \theta}{\partial z} \quad (37)$$

where $\mathcal{L}$ is an arbitrary length. The dimensionless fluxes read

$$\tilde{J}_m = \int_{\tilde{r}_i}^{\tilde{r}_o} \tilde{v}_z\, \tilde{r}\, \mathrm{d}\tilde{r}, \qquad \tilde{J}_e = \int_{\tilde{r}_i}^{\tilde{r}_o} \tilde{q}_z\, \tilde{r}\, \mathrm{d}\tilde{r}, \qquad (38)$$

For the sake of consistency with Ref. [45], we set $\mathcal{L} = r_o / \tilde{r}_o$ in Eq. (37) and $\ell = r_o$ in Eq. (24). After straightforward manipulation dimensionless mass and heat flow rates can be obtained from Eq. (36) as,

$$\tilde{m} = -\frac{2\dot{m}}{\pi r_o^2 \rho_0 \sqrt{2\theta_0}\, \tau} = \frac{4}{\tilde{r}_o^3}\int_{\tilde{r}_i}^{\tilde{r}_o} \tilde{v}_z\, \tilde{r}\, \mathrm{d}\tilde{r} \qquad (39)$$

$$\tilde{e} = -\frac{2\dot{e}}{\pi r_o^2 p_0 \sqrt{2\theta_0}\, \tau} = \frac{4}{\tilde{r}_o^3}\int_{\tilde{r}_i}^{\tilde{r}_o} \tilde{q}_z\, \tilde{r}\, \mathrm{d}\tilde{r} \qquad (40)$$

In the kinetic simulations [45], a rarefaction parameter δ is defined, that is related to our definition of Knudsen number [cf. Eq. (25)] via $\delta = 1/(\sqrt{2}\,Kn)$.

In Fig. 4, variations of dimensionless mass flow rate $\tilde{m}$ and heat flow rate $\tilde{e}$, with respect to Knudsen number are plotted for $\chi = 1$ and $\varepsilon = \{0.175, 0.523, 0.872\}$. NSF and R13 results are compared to kinetic data from linearized Boltzmann (LB) model [45], shown by symbols. As expected, both mass and heat flow rates increase when the diameter of the inner cylinder decreases, since larger values for ε correspond to narrower annuli. The solution for a cylindrical tube [12] can be obtained for $\varepsilon \to 0$ (not shown here). As depicted, R13 accurately predicts mass and heat flow rate for $Kn \leq 0.5$, whereas NSF fails to follow the kinetic data for mass flow rate. NSF results are acceptable only for heat flow rate at small Knudsen numbers, i.e., $Kn < 0.07$. At $Kn = 0.5$ the error of R13 results

with respect to kinetic data, evaluated from error = (data − model) / model, is about 7% for mass flow rate, and 11% for heat flow rate.
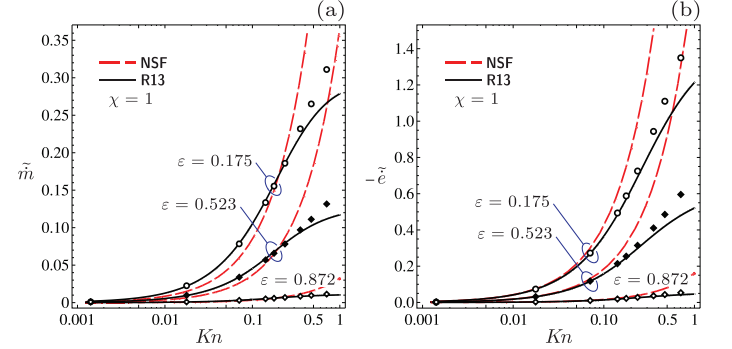
Fig 4: Variations of dimensionless mass flow rate $\tilde{m}$ and heat flow rate $\tilde{e}$ with respect to Knudsen number are shown for $\chi = 1$ and $\varepsilon = \{0.175, 0.523, 0.872\}$. R13 and Navier−Stokes−Fourier (NSF) results are compared to kinetic data (symbols) of linearized Boltzmann model [45].

As suggested by the analytical solutions (32)-(34), presence of Knudsen boundary layers in the R13 solutions, beside its accurate boundary conditions are the main reasons for priority of R13 over NSF system.

More comparison is performed in Fig. 5, where mass and heat flow rates from both BGK and LB kinetic models [45] are compared to our macroscopic results for a narrow and a wide annuli, $\varepsilon = \{0.175, 0.872\}$, with $\chi = 1$. In the transition regime where $Kn < 1$, our results agree with the trend in kinetic data. Compared to BGK model, LB model yields higher values for $\tilde{m}$ and $\tilde{e}$, because velocity and heat flux have larger magnitudes in the LB predictions, see Fig. 2.
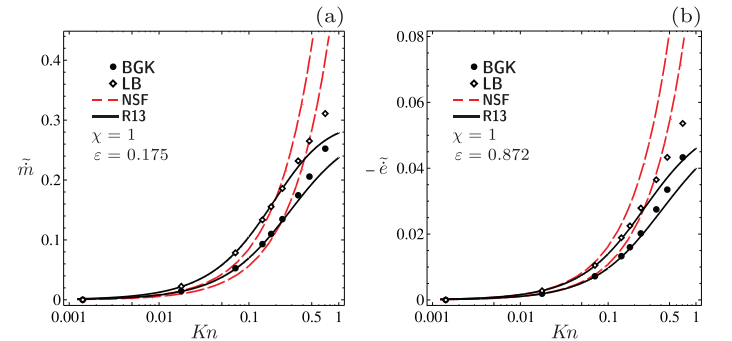
Fig. 5: Variations of dimensionless mass flow rate $\tilde{m}$ and heat flow rate $\tilde{e}$ with respect to Knudsen number are shown for $\chi = 1$ and $\varepsilon = \{0.175, 0.872\}$. R13 and Navier−Stokes−Fourier (NSF) results are compared to kinetic data of linearized Boltzmann model (diamonds) and BGK model (circles) from Ref. [45].

7. CONCLUSION

A compact analytical model based on the regularized 13-moment (R13) equations was employed to describe thermal transpiration flow of rarefied gases in tubes with annular cross section. Thermally-driven flows, forced by small temperature gradients were investigated with linearized equations, where

their solutions linearly depend on the temperature gradient. The effects of gas rarefaction, annulus geometry, and surface accommodation on the solutions of shear stress, heat flux, and velocity were examined.

Comparison of R13 solutions with kinetic data revealed that the dominant rarefaction effects in the considered flow are, (i) formation of Knudsen boundary layers, and (ii) slip velocity on the walls. The effects of these nonequilibrium phenomena on mass and heat flow rates are thoroughly demonstrated, and compared to high-quality Boltzmann simulations. Our comparisons confirm that the R13 system successfully approximates kinetic solutions for $Kn < 0.5$.

By comparing Navier–Stokes–Fourier (NSF) and R13 solutions, it is evident that Knudsen layers and their contribution on velocity slip are absent in the NSF theory; this is where the real advantage of R13 stands out. We highlighted the consequence of these shortcomings in NSF equations by computing mass and heat flow rates, and showed that NSF are valid in the slip flow regime.

To conclude, we point to the insufficiency of R13 equations for the description of highly rarefied flows $Kn \simeq 1$, in which the magnitude of rarefaction effects is beyond the resolution of R13 equations. In such conditions, larger systems of moment equations [49] are suggested.

ACKNOWLEDGEMENT

REFERENCES

[1]   Sone Y., 2000, "Flows induced by temperature fields in a rarefied gas and their ghost effect on the behavior of a gas in the continuum limit," Annu. Rev. Fluid Mech., **32**, p. 779.

[2]   Sone Y., 2002, Kinetic theory and fluid dynamics, Birkhäuser, Boston.

[3]   Reynolds O., 1879, "Experimental researches on thermal transpiration of gases through porous plates and on the law of transpiration and impulsion," Phil. Trans. Roy. Soc. Lon., **170**, p. 727.

[4]   Maxwell C., 1879, "On stress in rarefied gases arising from inequalities of temperature," Phil. Trans. Roy. Soc. Lon., **170**, p. 231.

[5]   Knudsen M., 1910, "Eine Revision der Gleichgewichtsbedingung der Gase. Thermische Molekularströmung," Ann. Phys., **31**, p. 205.

[6]   Knudsen M., 1910, "Thermischer Molekulardruck der Gase in Röhren," Ann. Phys., **33**, p. 1435.

[7]   Liang S. C., 1951, "Some Measurements of Thermal Transpiration," Journal of Applied Physics, **22**(2), p. 148.

[8]   Takaishi T., and Sensui Y., 1963, "Thermal transpiration effect of hydrogen, rare gases and methane," Trans. Faraday Soc., **59**, p. 2503.

[9]   Edmonds T., and Hobson J. P., 1965, "A Study of Thermal Transpiration Using Ultrahigh-Vacuum Techniques," J. Vac. Sci. Technol. A, **2**, p. 182.

[10]   Watkins R. A., Taylor W. L., and Haubach W. J., 1967, "Thermomolecular Pressure Difference Measurements for Precision Helium - 3 and Helium - 4 Vapor-Pressure Thermometry," The Journal of Chemical Physics, **46**, p. 1007.

[11]   Porodnov B. T., Kulev A. N., and Tukhvetov F. T., 1978, "Thermal transpiration in a circular capillary with a small temperature difference," J. Fluid Mech., **88**, p. 609.

[12]   Taheri P., and Struchtrup H., 2010, "An extended macroscopic transport model for rarefied gas flows in long capillaries with circular cross section," Physics of Fluids, **22**, p. 112004.

[13]   Vargo S. E., Muntz E. P., Shiflett G. R., and Tang W. C., 1999, "Knudsen compressor as a micro- and macroscale vacuum pump without moving parts or fluids," Papers from the 45th National Symposium of the American Vacuum Society, AVS, p. 2308.

[14]   Han Y.-L., Muntz E. P., Alexeenko A., and Young M., 2007, "Experimental and computational studies of temperature gradient-driven molecular transport in gas flows through nano/microscale channels," Nano. Microscale Thermophys. Eng., **11**, p. 151.

[15]   York D. C., Chambers A., Chew A. D., and Troup A. P., 1999, "Measurement of thermal transpiration across an array of parallel capillaries using a differential capacitance manometer," Vacuum, **55**, p. 133.

[16]   Struchtrup H., 2005, Macroscopic transport equations for rarefied gas flows: Approximation methods in kinetic theory, Springer, New York.

[17]   Loyalka S. K., 1971, "Kinetic theory of thermal transpiration and mechanocaloric effect. I," J. Chem. Phys., **55**, p. 4497.

[18]   Loyalka S. K., 1974, "Comments on Poiseuille flow and thermal creep of a rarefied gas between parallel plates," Phys. Fluids, **17**, p. 1053.

[19] Loyalka S. K., 1975, "Kinetic theory of thermal transpiration and mechanocaloric effect. II," J. Chem. Phys., **63**, p. 4054.

[20] Loyalka S. K., Petrellis N., and Storvick T. S., 1979, "Some exact numerical results for the BGK model: Couette, Poiseuille and thermal creep flow between parallel plates," J. Appl. Math. Phys. (ZAMP), **30**, p. 514.

[21] Barichello L. B., Camargo M., Rodrigues P., and Siewert C. E., 2001, "Unified solutions to classical flow problems based on the BGK model," J. Appl. Math. Phys. (ZAMP), **52**, p. 517.

[22] Ohwada T., Sone Y., and Aoki K., 1989, "Numerical analysis of the Poiseuille and thermal transpiration flows between two parallel plates on the basis of the Boltzmann equation for hard-sphere molecules," Phys. Fluids A, **1**, p. 2042.

[23] Loyalka S. K., and Hickey K. A., 1991, "Kinetic theory of thermal transpiration and the mechanocaloric effect: Planar flow of a rigid sphere gas with arbitrary accommodation at the surface," J. Vac. Sci. Technol. A, **9**, p. 158.

[24] Sone Y., and Yamamoto K., 1968, "Flow of rarefied gas through a circular pipe," Phys. Fluids, **11**, p. 1672.

[25] Loyalka S. K., 1969, "Thermal transpiration in a cylindrical tube," Phys. Fluids, **12**, p. 2301.

[26] Porodnov B. T., and Tukhvetov F. T., 1979, "Theoretical investigation of nonisothermal flow of a rarefied gas in a cylindrical capillary," J. Eng. Phys. Thermophys., **36**, p. 61.

[27] Lo S. S., Loyalka S. K., and Storvick T. S., 1984, "Kinetic theory of thermal transpiration and mechanocaloric effect. V. Flow of polyatomic gases in a cylindrical tube with arbitrary accommodation at the surface," J. Chem. Phys., **81**, p. 2439.

[28] Valougeorgis D., and Thomas J. R., 1986, "Exact numerical results for Poiseuille and thermal creep flow in a cylindrical tube," Phys. Fluids, **29**, p. 423.

[29] Sharipov F., 1996, "Rarefied gas flow through a long tube at any temperature ratio," J. Vac. Sci. Technol. A, **14**, p. 2627.

[30] Siewert C. E., 2000, "Poiseuille and thermal-creep flow in a cylindrical tube," J. Compu. Phys., **160**, p. 470.

[31] Sharipov F., 2003, "Application of the Cercignani-Lampis scattering kernel to calculations of rarefied gas flows. III. Poiseuille flow and thermal creep through a long tube," Eurp. J. Mech. B/Fluids, **22**, p. 145.

[32] Sharipov F., and Seleznev V., 1998, "Data on internal rarefied gas flows," J. Phys. Chem. Ref. Data, **27**, p. 657.

[33] Grad H., 1949, "On the kinetic theory of rarefied gases," Comm. Pure Appl. Math., **2**, p. 325.

[34] Grad H., 1958, "Principles of the kinetic theory of gases," *in* Handbuck der Phys., Vol. 12, S. Flugge, ed., Springer, Berlin.

[35] Chapman S., and Cowling T. G., 1970, The mathematical theory of nonuniform gases, Cambridge University Press, Cambridge.

[36] Struchtrup H., and Torrilhon M., 2003, "Regularization of Grad's 13-moment equations: Derivation and linear analysis," Phys. Fluids, **15**, p. 2668.

[37] Struchtrup H., 2004, "Stable transport equations for rarefied gases at high orders in the Knudsen number," Phys. Fluids, **16**, p. 3921.

[38] Torrilhon M., and Struchtrup H., 2004, "Regularized 13-moment equations: Shock structure calculations and comparison to Burnett models," J. Fluid Mech., **513**, p. 171.

[39] Taheri P., Torrilhon M., and Struchtrup H., 2009, "Couette and Poiseuille microflows: Analytical solutions for regularized 13-moment equations," Phys. Fluids, **21**, p. 17102.

[40] Taheri P., Rana A. S., Torrilhon M., and Struchtrup H., 2009, "Macroscopic description of steady and unsteady rarefaction effects in boundary value problems of gas dynamics," Cont. Mech. Thermodyn., **21**, p. 423.

[41] Taheri P., and Struchtrup H., 2009, "Effects of rarefaction in microflows between coaxial cylinders," Phys. Rev. E, **80**, p. 66317.

[42] Taheri P., and Struchtrup H., 2010, "Rarefaction effects in thermally-driven microflows," Physica A, **389**, p. 3069.

[43] Taheri P., and Struchtrup H., 2012, "Poiseuille flow of moderately rarefied gases in annular channels," Int. J. Heat Mass Transf., **55**, p. 1291.

[44] Torrilhon M., and Struchtrup H., 2008, "Boundary conditions for regularized 13-moment equations for micro-channel flows," J. Comp. Phys., **227**, p. 1982.

[45] Lo S. S., Loyalka S. K., and Storvick T. S., 1983, "Rarefied gas flow in a cylindrical annulus," J. Vac. Sci. Technol. A, **1**, p. 1539.

[46] Taheri P., 2010, "Macroscopic description of rarefied gas flow in the transition regime," PhD Thesis, University of Victoria.

[47] Torrilhon M., 2010, "Slow gas microflow past a sphere: Analytical solution based on moment equations," Physics of Fluids, **22**, p. 72001.

[48] Struchtrup H., and Torrilhon M., 2008, "Higher-order effects in rarefied channel flows," Phys. Rev. E, **78**, p. 46301.

[49] Gu X., and Emerson D. R., 2009, "A high-order moment approach for capturing non-equilibrium phenomena in the transition regime," J. Fluid Mech., **636**, p. 177.